THE FATIGUE DAMAGE BEHAVIOR OF A SINGLE CRYSTAL SUPERALLOY

Michael A. McGaw
National Aeronautics and Space Administration
Lewis Research Center
Cleveland, Ohio 44135

ABSTRACT

The uniaxial fatigue behavior of a single crystal superalloy, PWA 1480, is described. Both monotonic tensile and constant amplitude fatigue tests were conducted at room temperature, in an effort to assess the applicability of polycrystalline-based fatigue life prediction methods to a single crystal superalloy. The observed constant amplitude behavior correlated best using a stress-based life criterion. Nearly all specimens failed at surface or slightly subsurface microporosity; this is thought to be responsible for the unusually large amount of scatter in the test results. An additional term is developed in the stress-life equation for the purposes of accounting for the effect of microporosity on fatigue life. The form chosen is a function of the effective area of the failure-producing microporosity projected on a plane perpendicular to the loading axis, as well as the applied stress. This additional term correlated the data to within factors of two on life. Although speculative, extrapolation of the microporosity relation to zero micropore area indicates that approximately an order of magnitude improvement in fatigue life should result.

INTRODUCTION

The design of aircraft gas turbine and rocket engine structures, as well as many other similar structures involves calculation of the expected service lifetime. Turbomachinery components are generally subjected to fatigue cycling as a result of thermal, centrifugal and gas path loadings. High pressure turbine blades, for example, are service-life-limited by the effects of cyclic loading in the airfoil root and blade attachment areas.

Materials used in turbine engine hot section applications are the nickel-base superalloys (of various configurations, polycrystalline, Directionally Solidified and Single Crystal); they are extensively used in this application because of their superior strength and oxidation resistance properties at high temperatures. The advanced super-

alloys, the single crystal alloys, are being used in high performance turbomachinery applications. One such application where single crystal materials are being considered is in the turbine blading of the high pressure fuel turbopump of the NASA Space Shuttle Main Engine (SSME). In this case, the blade attachment region is cooled and hence is at a relatively low temperature with respect to the blade. The material being considered to replace current blading material is PWA 1480, a cast nickel-base single crystal superalloy proprietary to Pratt and Whitney Aircraft Corporation.

Current casting and processing techniques produce microporosity in single crystal materials; PWA 1480 is no exception. Surface and/or slightly subsurface microporosity is virtually always responsible for producing fatigue crack initiation in the low and intermediate temperature range [1, 2]. Consequently, it has been speculated that the use of processing techniques such as either hot-isostatic-pressing (hip) alone or in conjunction with high gradient solidification, both of which show promise in reducing or eliminating microporosity, would likely yield substantial improvements in the fatigue properties of this material [3,4,5].

The primary objective of this study is to determine the role of microporosity in fatigue life reduction at room temperature; a quantification of this role may provide a means of estimating improvements in fatigue properties in terms of the variables related to material processing. The secondary objective is to determine the applicability of polycrystalline life prediction methods to PWA 1480 single crystal alloy.

EXPERIMENTAL PROCEDURES

Material: PWA 1480

The material, PWA 1480 is a cast nickel-base superalloy whose composition is given in table 1. The specimens used in the study were machined from cylindrical castings approximately 3/4" in diameter and 6" in length. These castings were grown to within ten degrees of the [001] crystallographic direction with the secondary axis unspecified. Laue back-reflection x-ray techniques were used to determine crystal orientation. The cyclindrical castings were subjected to the following heat treatment schedule:

2345 °F in vacuum or protective atmosphere, 4 hours, rapid air cooled, and
1975 °F in protective atmosphere, 4 hours, air cooled.

Once the specimens were machined, an additional aging heat treatment consisting of

1600 °F in air, 32 hours, air cooled

was applied.

Microstructure:

The microstructure of this alloy, and specifically of this heat, was studied by Milligan [6]. He found that this alloy contained a fine dispersion of cuboidal gamma prime particles in a gamma matrix, with the primary gamma prime volume fraction approximately 55 to 60 %. This alloy also was found to contain a residual dendritic microstructure with interdendritic eutectic pools of approximately 5% volume fraction. The microporosity observed in this alloy occurs in the dendritic structure [6].

Microporosity Characterization:

Because microporosity occurs in the dendritic structure and since the dendrite formation is along the crystallograph growth axis for this orientation [1], longitudinal and transverse (with respect to the growth direction) specimens of material were characterized in terms of microporosity. The results are shown in figures 1, 2, and 3. Microporosity parameters of area fraction, maximum pore dimension and pore area were measured and are shown in table 2. While the average porosity features are relatively small, with the transverse direction features somewhat larger then those in the longitudinal direction, the variability in microporosity characteristics measured is quite large, for both sample directions. As can be observed, the maximum values observed are 4 to 8 times larger than the mean values.

Experimental Apparatus

The specimen geometry used in this study was a 1" uniform gage length solid cylindrical specimen with threaded ends. The diameter of the uniform test section was .25". Overall specimen length was approximately 4-1/2" (figure 4).

The equipment used to conduct the experimental phase of the research consisted of a servohydraulic materials testing system interfaced to a minicomputer system (figure 5) [7].

Experimental Procedures:

All tensile and low cycle fatigue baseline tests were conducted at room temperature under computer control using interrupt-driven, multitasked Pascal software [8].

RESULTS AND DISCUSSION

Results

Tensile Results:

Two tensile tests were performed so that variations in material behavior over the range of crystal orientations present could be assessed.

The orientations chosen corresponded to 1 and 10 degrees from the [001] direction; these orientations bracketed the orientations of the specimens to be tested in the experimental program. The loading modulus, yield strength and ultimate tensile strength values measured are presented in table 3. The stress-strain behavior of the specimen nearest the [001] direction showed a mild strain hardening character (figure 6a), while the specimen furthest away showed a virtually perfectly elasticplastic deformation behavior (figure 6b). This is in general qualitative agreement with the tensile behavior observed at 1000°F, although on a different heat of this material [9]. While the subject tests were conducted at room temperature, the qualitative comparison is valid, as the deformation mechanism for this material does not change from being highly inhomogeneous until approximately 1400°F [6,9].

Scanning electron micrographs of the fracture are presented in figure 7. The surfaces are rather uniform in appearance, with a much less crystallographic character than observed in fatigue.

Fatigue Results:

A total of sixteen tests were conducted, resulting in twelve valid data: two tests resulted in shoulder failures, the remaining two were considered runouts, that is, these specimens did not fail at the applied stress range for the duration of the test. The results are presented in table 4 and figures 8 and 9. As can be observed, considerable scatter, even within the context of the factors of two on life commonly accepted in fatigue studies, is present. Material stress-strain response was virtually stable at all strain ranges for the orientations tested, not an unexpected result based on the observed monotonic stressstrain behavior. The relatively low amounts of inelastic strain observed in the low cycle fatigue life range, together with the inhomogeneous nature of deformation in this material at this temperature, effectively precludes the use of inelastic strain-based life criteria (fig. 8). This does not mean, however, that the complete (elastic and inelastic) Manson-Coffin-Basquin equation does not necessarily apply to the observed behavior of this material; rather, it is the magnitude and nature of the inelastic strain observed at this temperature which makes the inelastic term negligibly small compared to the elastic term. Table 5 gives the results of fitting the Manson-Coffin-Basquin equation to the total and elastic strain, as well as the stress range, respectively, versus life data:

$$\Delta\varepsilon_T = A'(N_f)^{\alpha'} \quad \text{(1a)}$$

$$\Delta\varepsilon_E = A''(N_f)^{\alpha''} \quad \text{(1b)}$$

$$\Delta\sigma = A(N_f)^{\alpha} \quad \text{(1c)}$$

The data appear more consistent using a stress-based life criterion (fig. 9). The observed versus predicted fatigue life according to a stress-based life criterion is shown in figure 10, showing that while the data appear more consistent in this context, considerable scatter is present. The fracture appearance varied with the life level, although a common characteristic was a highly crystallographic appearance in all cases. The low cycle fatigue fractures were characterized by multiple slip plane facets, apparently indicative of many active slip systems induced by the large global strains. High cycle fatigue fractures were characterized by failure along one dominant plane: Ostensibly a {111} - type of octahedral shear plane. Majumdar, et. al., found a similar appearance in the results obtained in room temperature and higher temperature (1000 °F) tests [2].

In all but one test, the failure initiation zone was found to be at sites of surface-connected or slightly subsurface microporosity. In some cases, one micropore was responsible; in others, multiple micropores were present. Typical failure producing micropore sites are shown in figure 11. As can be seen from the figure, micropore morphology and orientation with respect to the specimen axis varies considerably. The two specimens which failed in the shoulder region did so due to microporosity within a region containing an usually large micropore concentration. The two runout specimens were examined for surface flaws; nothing unusual was found. It would appear that these specimens possessed micropore morphologies which coincidentally were either very small in the surface and near surface region, or substantially below the surface, so that their effect as stress concentrators and surface crack initiators would be reduced significantly.

Discussion

Tensile Behavior:

A reasonable approximation of the fatigue behavior of a metallic material can usually be obtained from a knowledge of the material's monotonic behavior, viz., ultimate tensile strength, modulus of elasticity and fracture ductility, used in conjunction with the Method of Universal Slopes, proposed by Manson and Hirschberg [10]. This method, which was developed from the analysis of fatigue and tensile data for a large number of polycrystalline materials, has the form of the Manson-Coffin-Basquin equation, wherein the exponents of the two power law terms are given "universalized" values:

$$\Delta\varepsilon_t = D^{0.6} N_f^{-0.6} + \frac{3.5\,\sigma_{UTS}}{E} N_f^{-0.12} \qquad (2)$$

In making application of this method to single crystal materials, it is reasonable to expect that an equation of this type could be utilized for estimating fatigue behavior, changes of the "universalized constants" or minor variations of the functional form notwithstanding.

The predicted fatigue behavior of this material using the Method of Universal Slopes is shown together with the observed fatigue behavior, in figure 12 (the ductility was estimated from data in [12]). It is apparent that at this temperature, a very good estimate of this alloy's fatigue behavior can be obtained by using monotonic tensile properties.

Fatigue Behavior:

The relatively large amount of scatter (greater than a factor of two on life) in the fatigue results, together with the observation that in virtually every case, fatigue failure initiated at sites of micro-porosity, provide motivation for examining in greater detail the effects of microporosity on failure behavior.

One approach to this problem is to consider the presence of micropores as starter cracks and, in view of the fact that the global stress-strain behavior for all tests was virtually elastic, apply Linear Elastic Fracture Mechanics (LEFM) principles, thus treating the failure behavior as a crack growth problem. An advantage of this approach is that the cumulative loading problem can be treated in a much more straight forward manner by using a linear cumulative damage law, although threshold and retardation effects limit the applicability of treatment. Majumdar and Kwasny used this approach to treat the fully-reversed high cycle fatigue and mean stress fatigue experiments they performed under contract to NASA [2]. While Majumdar and Kwasny applied LEFM methods to the analysis of their test results, their goal was the modeling of mean stress fatigue behavior, not the consideration of the influence of microporosity on fatigue behavior and the attendant scatter in results it produces. As a consequence, one of the assumptions they made in performing the analysis ignores considerations of microporosity (initial flaw) size variation. Never-the-less, given the fact that microporosity was responsible for failure in virtually all baseline fatigue test results, an expression for describing the effect of microporosity on fatigue life behavior based upon or at least guided in part by LEFM arguments appears plausible.

A number of difficulties, however, impede an approach based strictly on LEFM principles:

1. An expression for the stress intensity factor is difficult to determine; fracture surfaces examined in this study as well as those reported in [2] would indicate mixed mode (I and II) crack growth. This is in addition to the fact that the material of interest is anisotropic.

2. Little, or little easily obtainable crack growth data for this material exists, making estimates of the threshold stress intensity, Paris law constants, etc. difficult to determine.

3. A difficulty in handling the initiation life exists; as pointed out in [2], detailed metallurgical studies at various fractions of life would have to be made to make a determination.

4. While the bulk of the test results show that nominally elastic response is obtained in most cases, small but finite inelastic strains are observed for many of the lower life results, creating the additional complication of having to address inelastic strain fields around micropore defects. This concern may well extend to other medium life results as well, since while the global stress-strain behavior is nominally elastic, the stress field local to the micropore site may be great enough to produce inelastic deformation.

Because of these difficulties, a somewhat more empirically-based approach was taken.

First attempts at accounting for this influence were to treat the micropore sites as "effective cracks", and using a knowledge of the theoretical stress concentration factor solution for a uniform round bar (semi-elliptical crack) under tension to develop a basis for constructing the fatigue life dependence [11]. Various strategies were pursued, the most obvious being to treat the micropore sites as semi-elliptical cracks by enclosing the sites by ellipses, and then measuring the major and the minor axes of the ellipses for use in data analyses. Another strategy was based on the observation that the solution for the effective stress concentration factor involved the major and minor ellipse axes, and therefore, ellipse area, leading to analyses involving "effective area." Neither of these approaches led to reasonable correlations.

Since efforts which treated the micropore sites as stress concentrations in a more ideal sense failed to yield results, somewhat more pragmatic approaches were followed, including examination of micropore site depth and projected effective micropore site area normal to the loading axis. In this case, the effective micropore site area is defined as the aggregate area of all micropores present in the initiation zone. The object of the analysis was to search for a function involving effective micropore area which would increase or decrease life, e.g.:

$$\Delta\sigma = (f(A_p)\ N_f)^{\alpha} \tag{3a}$$

or

$$\frac{(\Delta\sigma)^{1/\alpha}}{N_f} = f(A_p) \tag{3b}$$

Figure 13 is a plot the left-hand side of equation 3b, where α can be taken as obtained in the previous fatigue regression results,

versus the effective micropore site area. The function plotted is linear in effective micropore site area. Note that a stress range dependence is apparent: Data above the curve possess, for the most part, stress ranges which are smaller than those data below the curve. Subsequent analyses led to a reasonable correlation using a function involving the applied stress range and the effective micropore site area projected normal to the loading axis (table 6, fig. 14). The measure of effective micropore site area is an aggregate, approximate one - aggregate in that the majority of cases, multiple micropores were present in the initiation site and are collectively connected to form one effective "micropore;" approximate in the sense that the actual micropores are complex three dimensional objects lying in a more or less random orientation with respect to the crystallographic growth the direction. Moreover, the areas measured are those obtained from SEM photographs of the fracture surface - a small number of photos featured the specimen axis tilted somewhat so that the failure initiating micropore site could be more clearly delineated. In those photographs then, the projected micropore area normal to the specimen axis and that measured from the photograph differ somewhat. Because of the complex geometry of the micropores (they often wind into and out of the fracture surface), it is felt that the area measurements obtained in this manner are reasonably valid. The measure of effective micropore area is, after all, a first approximation of the stress-intensification effects of the micropore sites. The precise form of the function chosen to model the data shown in figure 14, is:

$$\Delta\sigma = \left\{ \left[a + b \left(A_p / \Delta\sigma \right) \right] N_f \right\}^{\alpha} \qquad (4)$$

This equation has a number of features making it better suited for use in this case than other possible forms; these include:

1. When effective micropore area is zero, a finite life relationship is still obtained.

2. For a given stress range, as effective micropore area decreases, (with b positive) fatigue life increases, lessening micropore influence.

The first feature is perhaps the more subtle of the two, but has interesting speculative implications for the use of an equation of such a form. This functional form leads to the conceptually consistent result that if the effective micropore area is decreased to zero, a finite life relation exists, meaning that, if a micropore is present at or near the surface, it will be the dominant life-limiting feature. If such a micropore feature does not exist,a finite, though greater, life is still expected, and the failure will presumably be due to another cause.

The fatigue data, reinterpreted in accordance with the above equation are presented in figure 15. It can be seen that the use of equation 4 collapses the scatter compared to the unprocessed data shown previously in figure 10, to within factors of two. On the speculation that if micropore area was decreased to zero, improvements in fatigue life of approximately one order of magnitude (corresponding to a 36% increase in fatigue strength) are predicted (figure 16). This result provides great impetus for the development of processing techniques which take advantage of the theoretically possible improvements in fatigue properties. The observation of runout data relative to the zero micropore stress-life line (figure 16) is of interest. It can be observed that the runout data exhibited a minimum cyclic capability less than that of which would be predicted for a "micropore free" material, suggesting that the proposed model of micropore influence is capturing the first order effects; of course, these are still runout tests and failure must occur at lives equal to or greater than that predicted by the current zero micropore prediction. Additional data in this region would be required to establish a more accurate determination of the micropore model parameters.

Majumdar and Kwasny [2], although ignoring variation in the initial defect (micropore) size in interpreting their results did, however, speculate on what improvements may be expected if microporosity size were reduced. They found that predictions of early high cycle fatigue life improvement of approximately an order of magnitude could be obtained if the micropore size responsible for producing failure were reduced from 40 μm to 10 μm. Two problems are apparent from their analysis, however: The first is that theirs is an LEFM analysis and the shrinking of the initial flaw (micropore) size to zero results in a prediction of infinite life regardless of stress level (c.f. equation 10 in [2]), a physically untenable result. The second issue concerns the difficulties in the determination of the threshold stress intensity, as discussed earlier.

Examination of table 6 with respect to effective micropore area and maximum micropore dimension (dimension of the micropore possessing the maximum dimension in the aggregate micropore site) reveals that the average micropore area (defined as the effective micropore area divided by the number of micropores contributing to the area) as well as the maximum micropore dimension are significantly larger than those parameters as measured by a routine microporosity characterization as described earlier. Specifically, the average micropore area in the failure site was found to be 5003 (μm^2), with a standard deviation of 2532 (μm^2), while the average maximum micropore dimension was found to be 192 (μm), with a standard deviation of 83 (μm). Comparing these values with those obtained in the microporosity characterization for this material (e.g., table 2) shows that the micropores responsible for failure are approximately five to ten times larger in terms of the maximum micropore dimension and approximately

twenty to thirty times larger in terms of the average micropore area. Note that the standard deviations for the measurements in table 2 are very large compared to the mean, while the standard deviations of the failure specimen micropore measurements are approximately half of the mean values. This comparison should be put into perspective, however; the data in table 2 are the result of measurements taken from sections arbitrarily selected from within the specimen bulk, while the failure micropore data are not nearly so arbitrary: These data have been in a sense "screened" by the fatigue damage process. The fatigue damage process will always choose the most deleterious defect region to produce failure. For this material at the temperature tested, this refers to the surface-connected and slightly subsurface microporosity sites. If a relation between the mean micropore size (preferably in terms of micropore area) as measured in standard characterization tests and, as obtained in fatigue could be obtained, then one is closer to predicting the fatigue properties of this material in terms of those processing variables affecting microporosity creation.

Finally, we are left with the fact that orientation may play a role in the effect of microporosity: deviation from the [001] crystallographic growth direction affects the material stress-strain behavior as observed in the monotonic tensile experiments, and very likely affects the fatigue behavior. Further, the dendritic structure which contains the microporosity is a function of orientation: It is known, for example, that the dendritic structure of this material as grown in the [001] direction is continuous along the [001] direction, while crystals grown in the [010] direction feature transverse planes of short secondary dendrite arms alternating with layers of microporosity and eutectic gamma prime [1]. While the material properties of strength and modulus are virtually identical for these two orientations, the dendritic structure difficiencies give rise to different fatigue characteristics; in this case, [001] orientations are superior to [010] orientations [1].

CONCLUSIONS

1. An additional term in the fatigue life relationship was developed for the purposes of predicting the effect of microporosity on fatigue life. The form presented is a function of the (failure) micropore area divided by the applied stress range. Use of this relationship correlated the baseline fatigue results to within factors of two scatter bands; residual variability is taken to be the sum of three elements: First, orientation effects are not accounted for in the model presented; second, the use of an area parameter to characterize the stress-intensification capability of a micropore constitutes an error in that it is a gross measure of the extremely complex microporosity morphology present in this highly anisotropic material; lastly, a finite amount of variability in fatigue exists exclusive of microporosity effects.

2. For this material and crystallographic orientation, at the temperature tested, the monotonic tensile properties together with the Method of Universal Slopes gave a very good estimate of the fatigue behavior.

3. Although speculative, it is estimated by use of the microporosity model presented, that if (the failure) micropore area were reduced to zero, improvements in fatigue properties of approximately an order of magnitude in life would result. This corresponds to a predicted increase in the fracture stress of 36%.

REFERENCES

1. DeLuca, D. P.; Cowles, B. A.; "Fatigue and Fracture of Advanced Blade Materials," Air Force Wright Aeronautical Laboratories Report, AFWAL-TR-84-4167 (February 1985).

2. Majumdar, S.; and Kwasny, R.; "Effects of High Mean Stress on the High-Cycle Fatigue Life of PWA 1480 and Correlation of Data by Linear Elastic Fracture Mechanics," NASA CR-175057, 1985.

3. Khan, T.; and Caron, P.; "The Effect of Processing Conditions and Heat Treatment on the Mechanical Properties of a Single Crystal Alloy," ONERA TP 1985-15.

4. Harris, K.; Erickson, G. L.; and Schwer, R. E.; "Development of the CMSX Series of Single Crystal Alloys for Advanced Technology Turbine Components," Proceedings TMSAIME Fall Meeting, St. Louis, Missouri, October, 1982.

5. Dreshfield, R. L.; and Parr, R. A.; "Application of Single Crystal Superalloys to Earth-to-Orbit Propulsion Systems," NASA TM-89877, 1987.

6. Milligan, W. W.; "Yielding and Deformation Behavior of the Single Crystal Nickel-Base Superalloy PWA 1480," NASA CR-175100 (1986).

7. McGaw, M. A.; and Bartolotta, P. A.; "The NASA Lewis Research Center High Temperature Fatigue and Structures Laboratory," Proceedings of the 4th Annual Hostile Environments and High Temperature Measurements Conference, Society of Experimental Mechanics, March, 1987.

8. McGaw, M. A.; and Bonacuse, P. J.; "Automation Software for a Materials Testing Laboratory," Proceedings of the NASA Turbine Engine Hot Section Technology Conference, NASA CP 2444, 1986.

9. Miner, R. V. (private communication).

10. Manson, S. S.; "Fatigue: A Complex Subject - Some Simple Approximations," Proceedings, Society of Experimental Stress Analysis, Vol. 12, No. 2, 1965.

11. "Stress Intensity Factors Handbook," Y. Murakami, ed. Pergamon Press, Oxford, 1987.

12. Fritzemeir, L. G.; and Schnittgrund, G. D.; "Advanced Single Crystal for SSME Turbopumps," NASA Contractor Report for NASA Contract NAS3-24646, Rocketdyne Document No. BC 87-214, 1987.

Element	Weight Percent
Al	4.8
C	(42 ppm)
Co	5.3
Cr	10.4
Ta	11.9
Ti	1.3
W	4.1
Ni	Bal.

TABLE 1 - COMPOSITION OF PWA 1480

Microporosity Parameter	Mean	Std. Dev.	High Val.	Mean	Std. Dev.	High Val.
Area fraction (%)	0.29	0.31	1.33	0.36	0.41	1.96
Maximum Pore Dimension (μm)	14.9	15.7	68	20.4	20.2	143
Pore Area (μm^2)	172	279	1,425	252	324	925

Table 2. MICROPOROSITY PARAMETERS

Specimen No.	Orientation (degrees from [001])	E,*10^3Ksi	.2% Yield Strength, Ksi	Ultimate Tensile Strength, Ksi
76	1	16140	147.5	156.3
190	10	17310	141.4	141.4

TABLE 3. TENSILE PROPERTIES

Specimen No.	E,*10^3 Ksi	Orientation, Degrees from [001]	Stress Range, Ksi	Total Strain Range	Cycles-to-Failure, N_f
73	18166	7.5	258.10	0.015558	494
92	17806	7.5	227.40	0.015187	3230
102	17513	7.5	241.90	0.015293	2034
133	17948	4.0	76.00	0.004234	1175400
139	18775	3.0	105.00	0.005593	293100
143	17691	4.5	176.10	0.010319	4742
149	17900	4.0	85.00	0.004749	2178300
153	18728	3.0	70.00	0.003738	39197500
156	17945	7.0	206.60	0.012330	7188
157	18338	6.0	188.50	0.010372	5755
165	18956	3.0	140.00	0.007386	59800
172	18642	3.0	140.00	0.007510	182900
177	18346	4.5	85.66	0.004669	3405600
184	17996	4.0	76.00	0.004223	812100
185	17758	4.0	76.00	0.004280	2304300
187	18818	7.0	76.00	0.004039	49817700

Note: Specimen No.'s 153 and 187 are runouts; No.'s 133 and 184 are shoulder failures.

TABLE 4. FATIGUE TESTING SUMMARY

Life Criterion	Coefficient	Exponent
Total strain range	0.046028	-0.159458
Elastic Strain range	0.397197	-0.156981
Stress Range	653.871	-.139371

TABLE 5. POWER LAW PARAMETERS FOR PWA 1480

Specimen No.	Effective Micropore Area, μm^2	Number of MicroPores	Maximum Micropore Dimension, μm
172	4822	1	305
149	3950	1	148
156	6255	2	144
92	4670	2	108
102	9355	1	164
165	14187	3	301
185	8212	1	195
139	8543	3	132
157	8289	2	110
73	45385	5	279
143	23138	3	317
177	0	0	0

Note: Specimen No.'s 73 and 177 were considered outliers and are omitted from the micropore relation calculations.

TABLE 6. MICROPOROSITY CHARACTERISTICS OF THE FATIGUE RESULTS

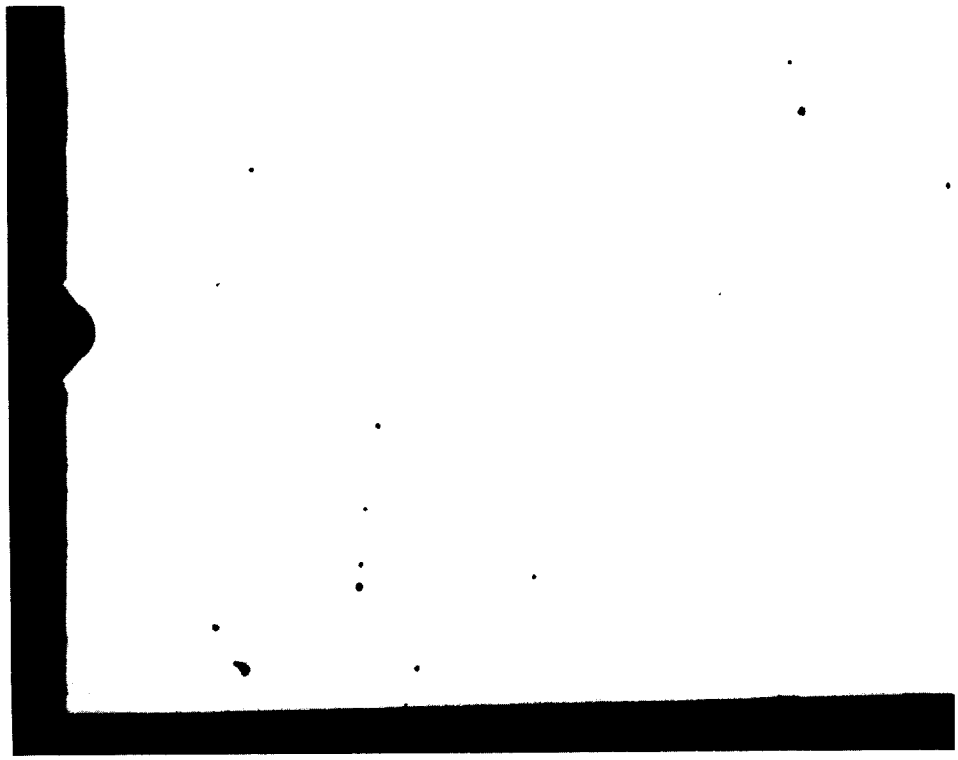

Figure 1a. Longitudinal Microporosity

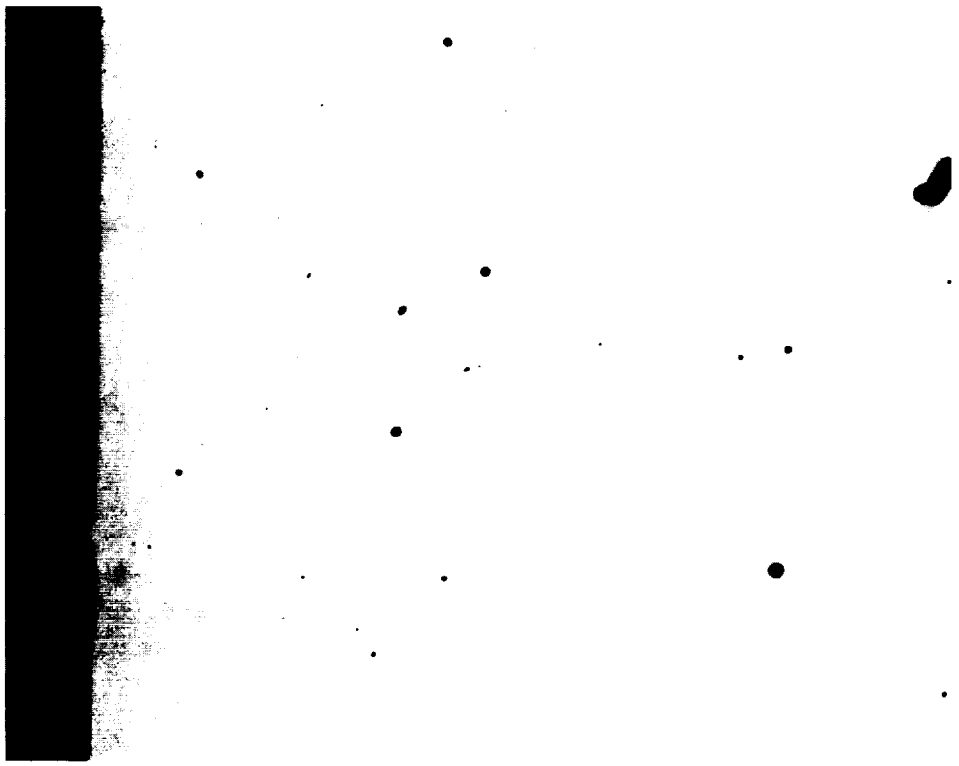

Figure 1b. Transverse Microporosity

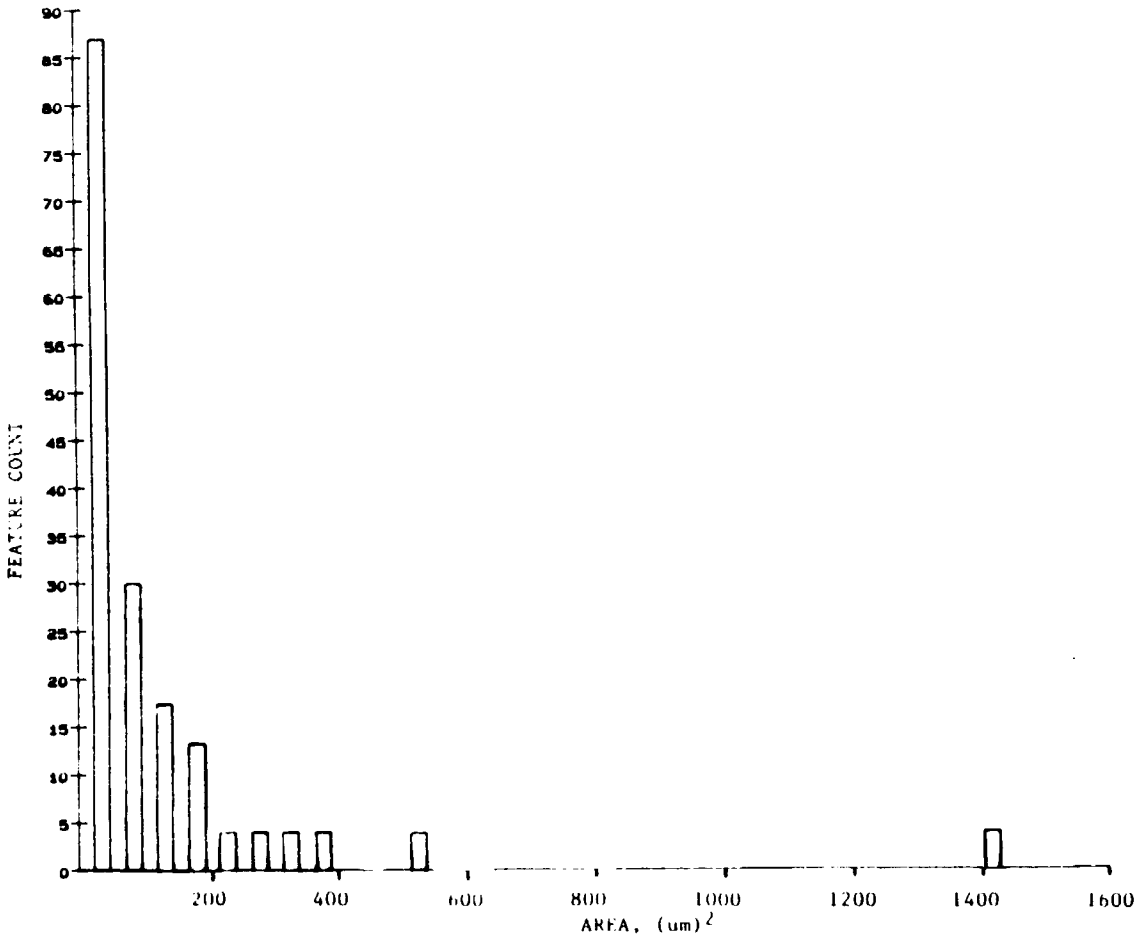

Figure 2a. Frequency Distribution of Microporosity, Longitudinal, Micropore Area

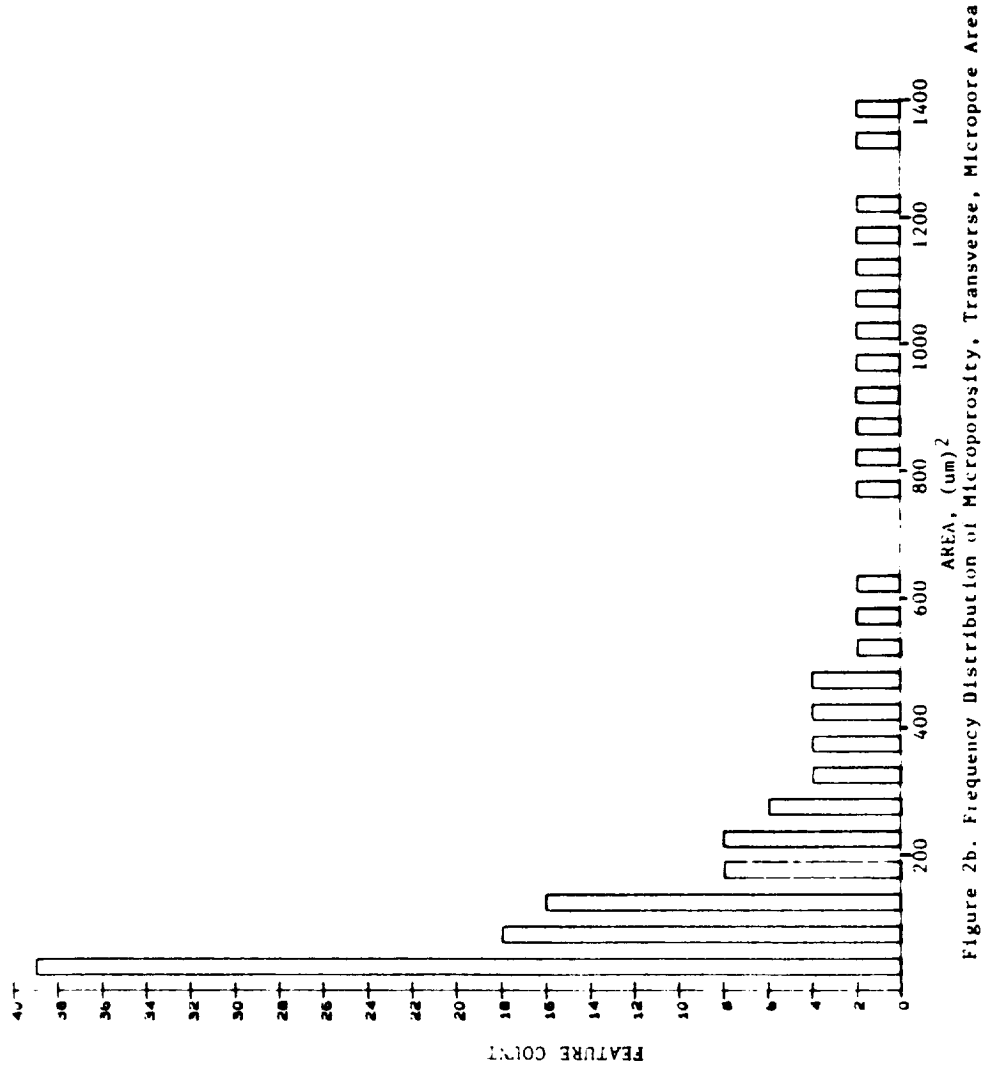

Figure 2b. Frequency Distribution of Microporosity, Transverse, Micropore Area

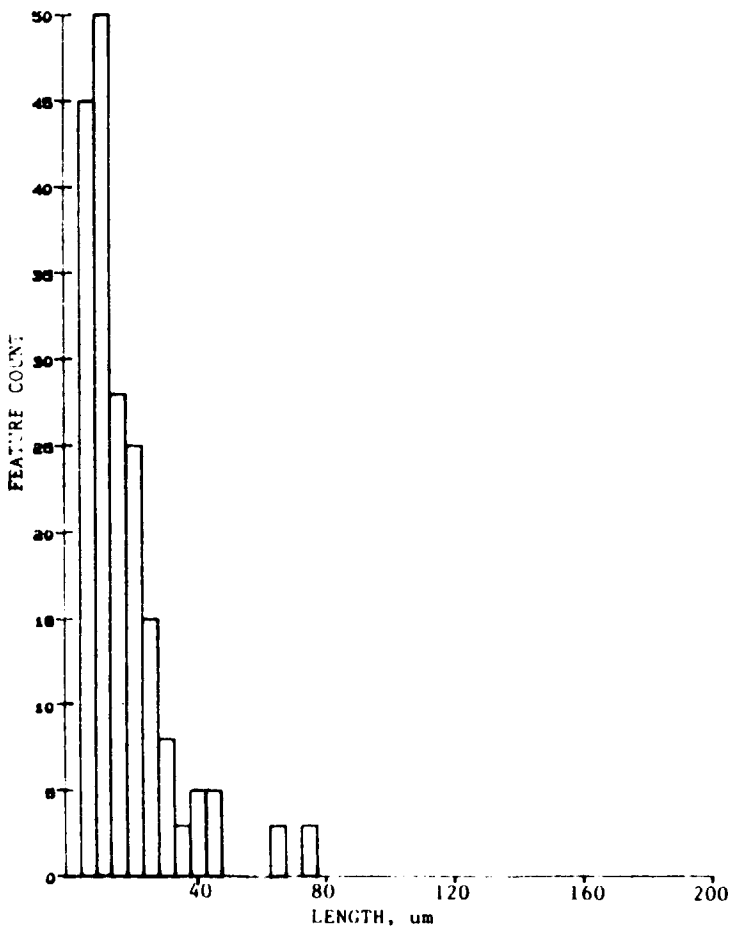

Figure 3a. Frequency Distribution of Microporosity
Longitudinal, Micropore Dimension

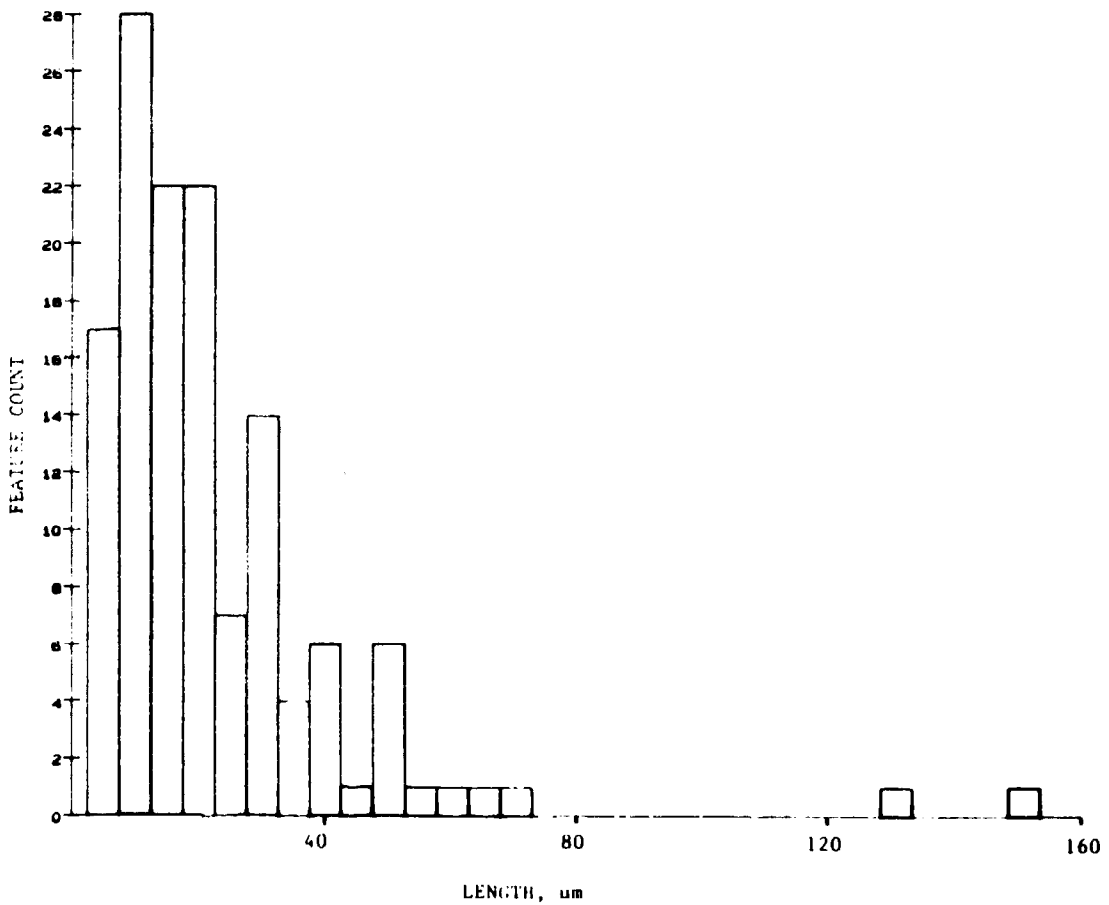

Figure 5b. Frequency Distribution of Microporosity, Transverse by Micropore Dimension

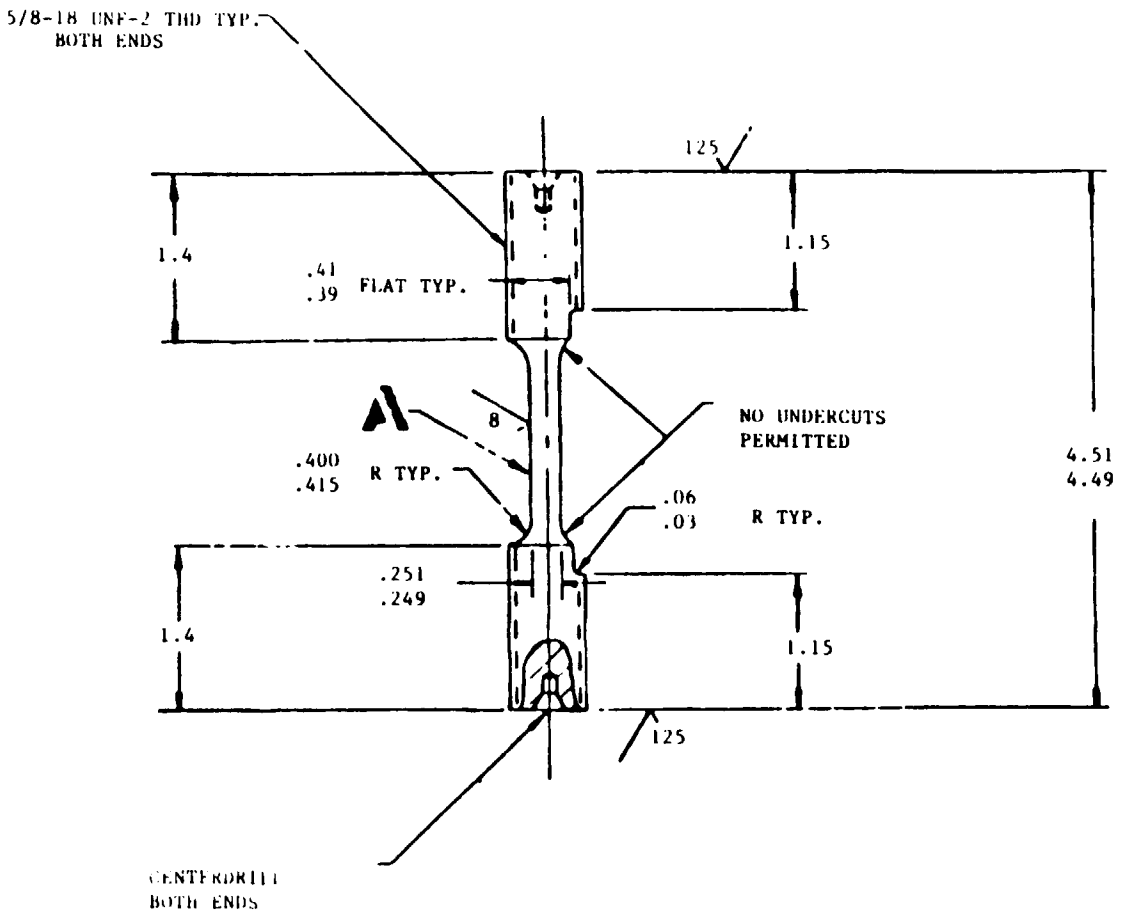

Figure 4. Specimen Geometry

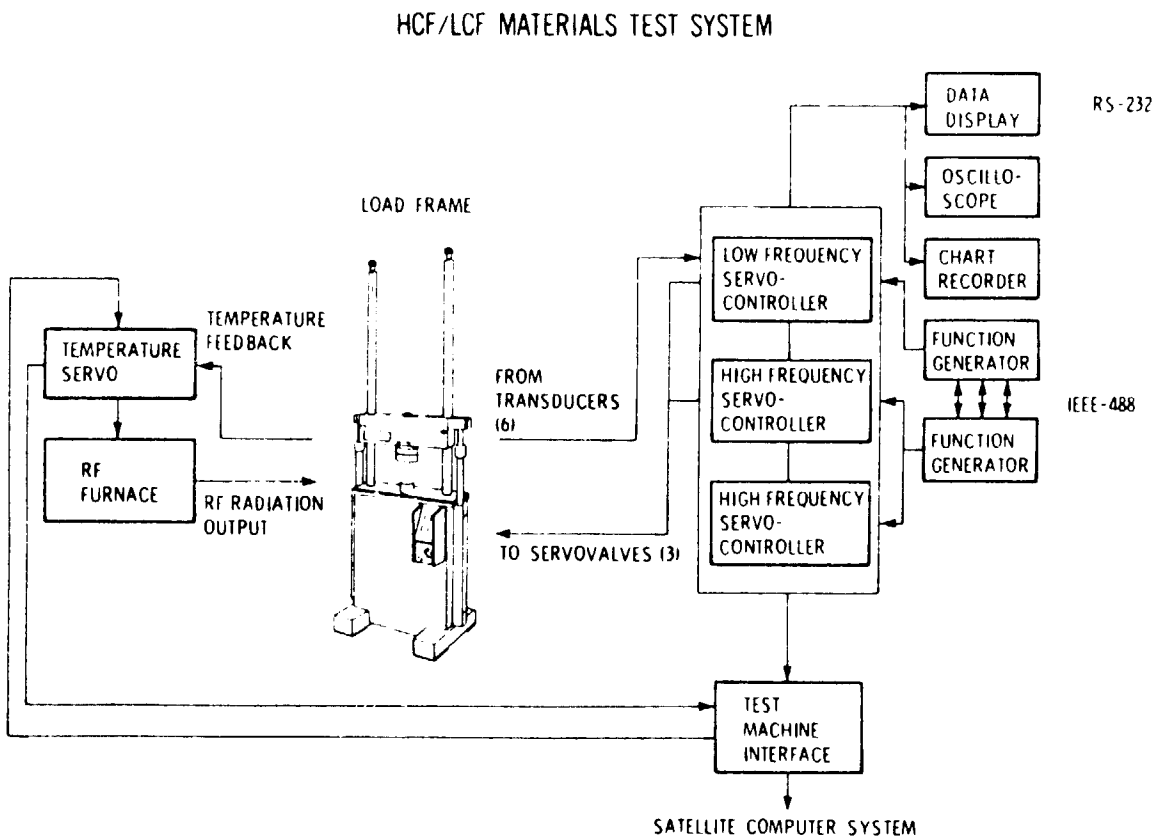
HCF/LCF MATERIALS TEST SYSTEM
DATA DISPLAY
RS-232
OSCILLO-SCOPE
CHART RECORDER
FUNCTION GENERATOR
IEEE-488
FUNCTION GENERATOR
LOAD FRAME
LOW FREQUENCY SERVO-CONTROLLER
HIGH FREQUENCY SERVO-CONTROLLER
HIGH FREQUENCY SERVO-CONTROLLER
TEMPERATURE FEEDBACK
TEMPERATURE SERVO
RF FURNACE
RF RADIATION OUTPUT
FROM TRANSDUCERS (6)
TO SERVOVALVES (3)
TEST MACHINE INTERFACE
SATELLITE COMPUTER SYSTEM

Figure 5

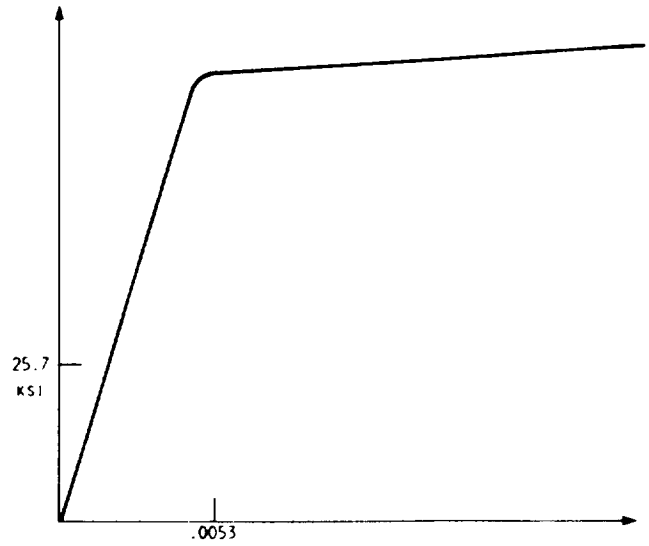

(A) 1 DEG FROM [001].

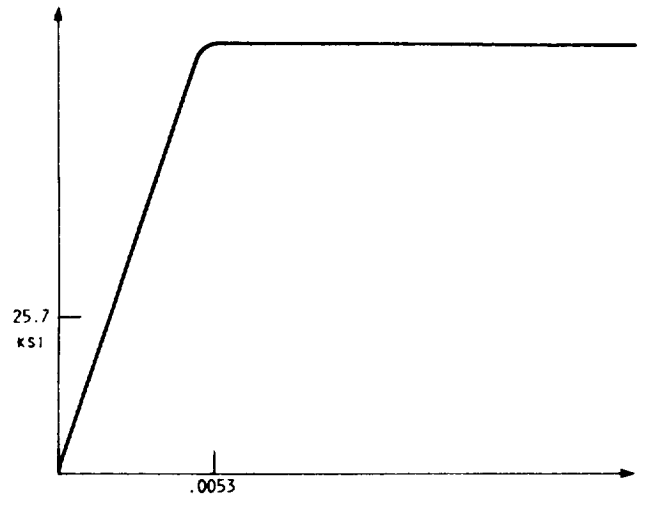

(B) 10 DEG FROM [001].

FIGURE 6. - MONOTONIC TENSILE BEHAVIOR.

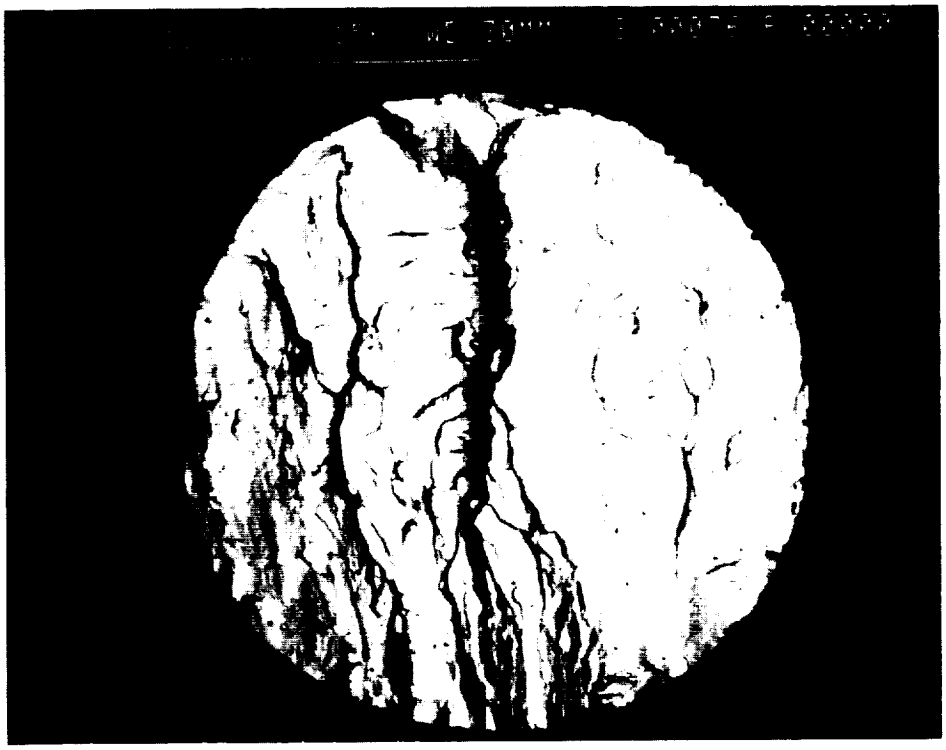

Figure 7a. Monotonic Tensile Fracture Surface: 1 Degree from [001]

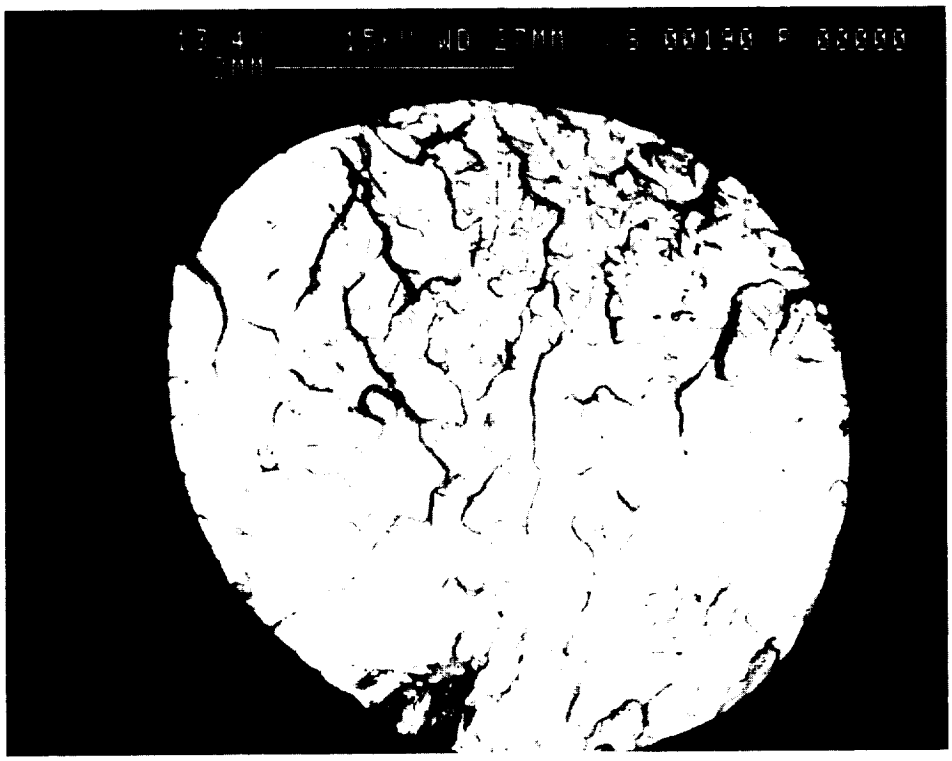

Figure 7b. Monotonic Tensile Fracture Surface: 10 Degrees from [001]

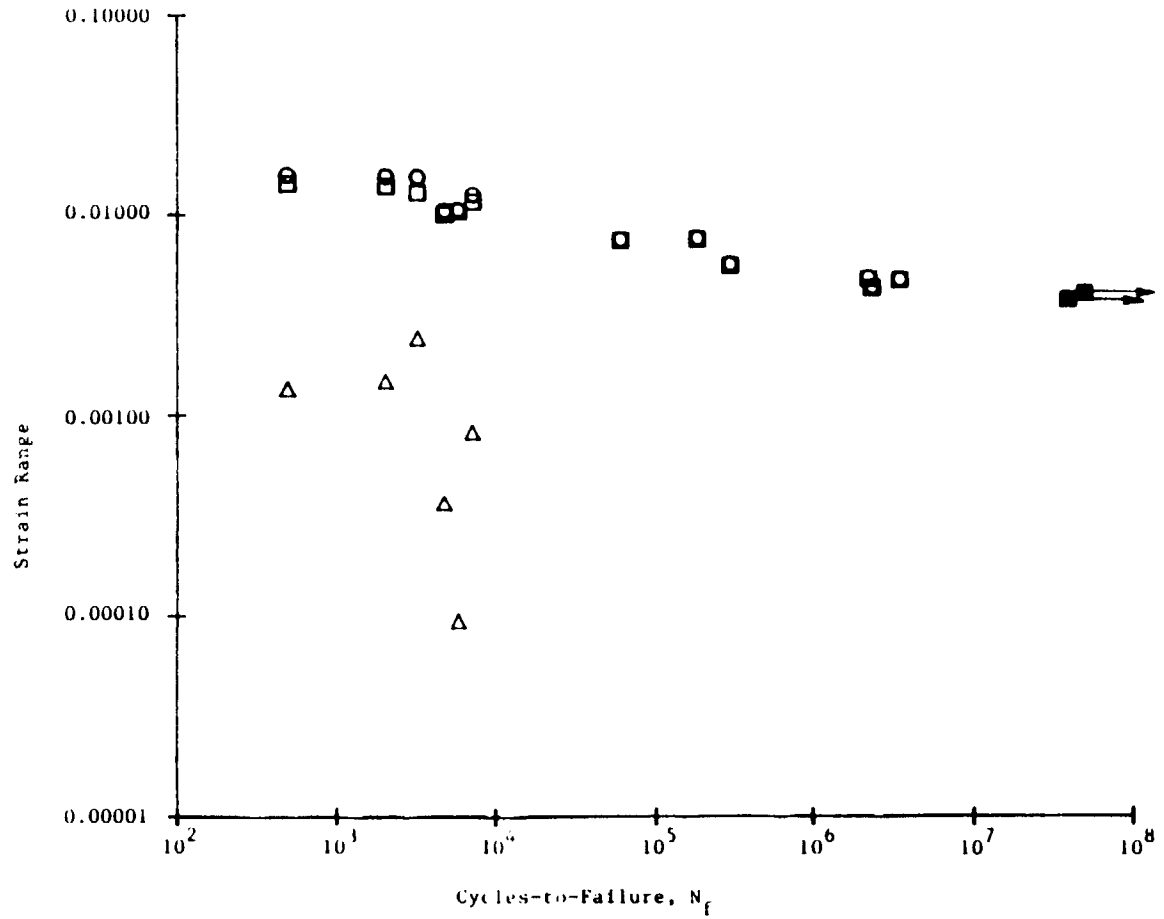

Figure 8. PWA 1480: Total Strain vs. Life

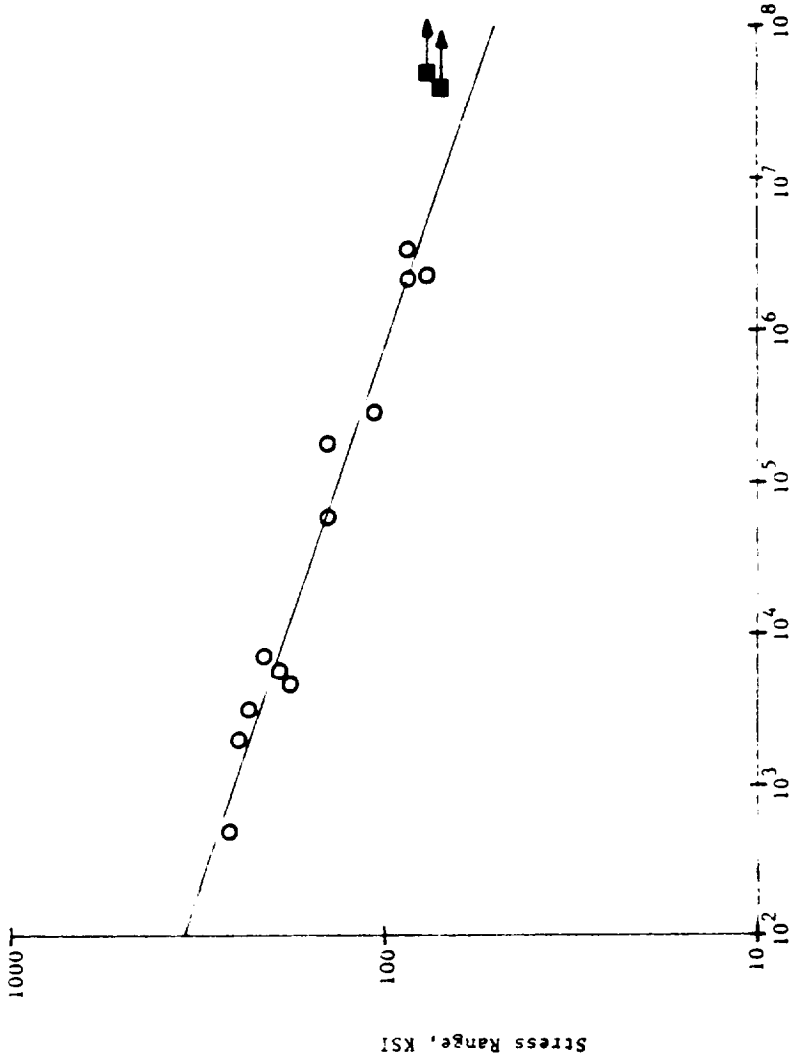

Figure 9. PWA 1480: Stress vs. Life

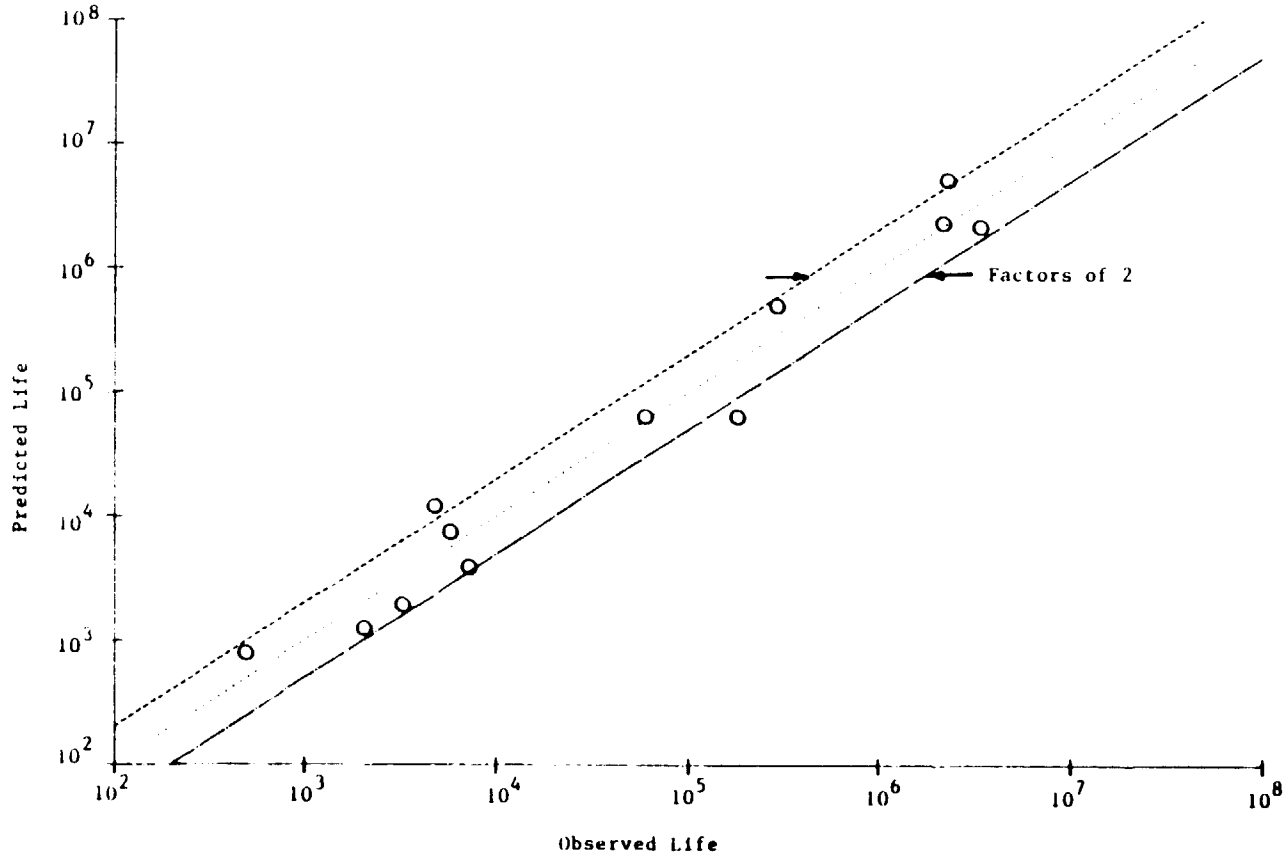

Figure 10. PWA 1480: Predicted vs. Observed Life, Stress-Based Criterion

Figure 11a. Variation in Failure Micropore Morphology

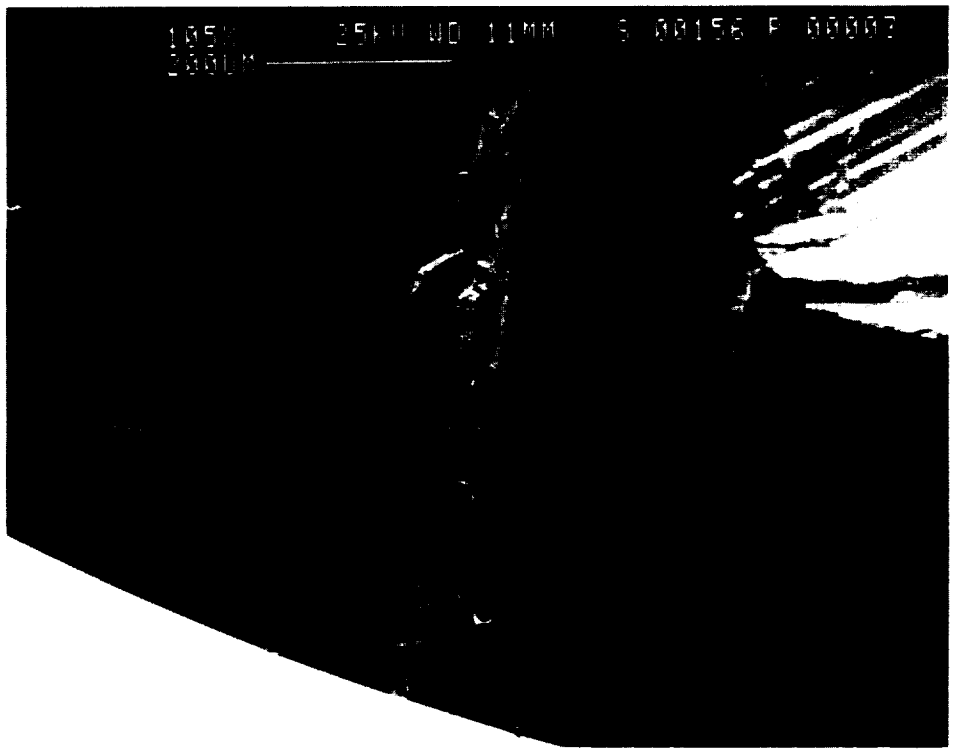

Figure 11b. Variation in Failure Micropore Morphology

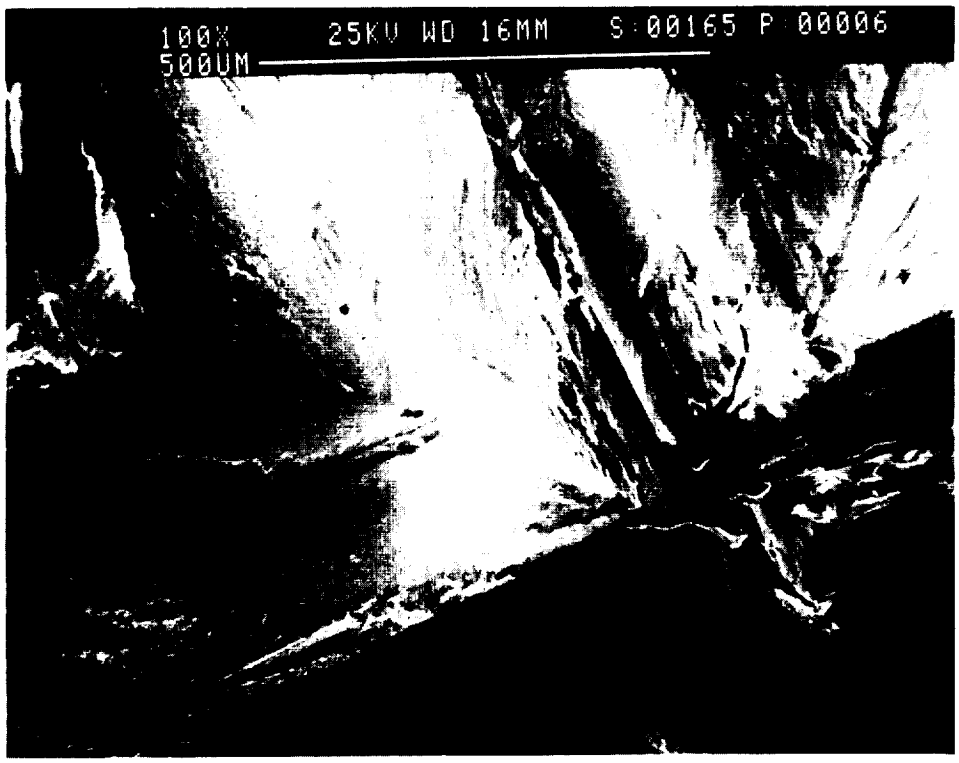

Figure 11c. Variation in Failure Micropore Morphology

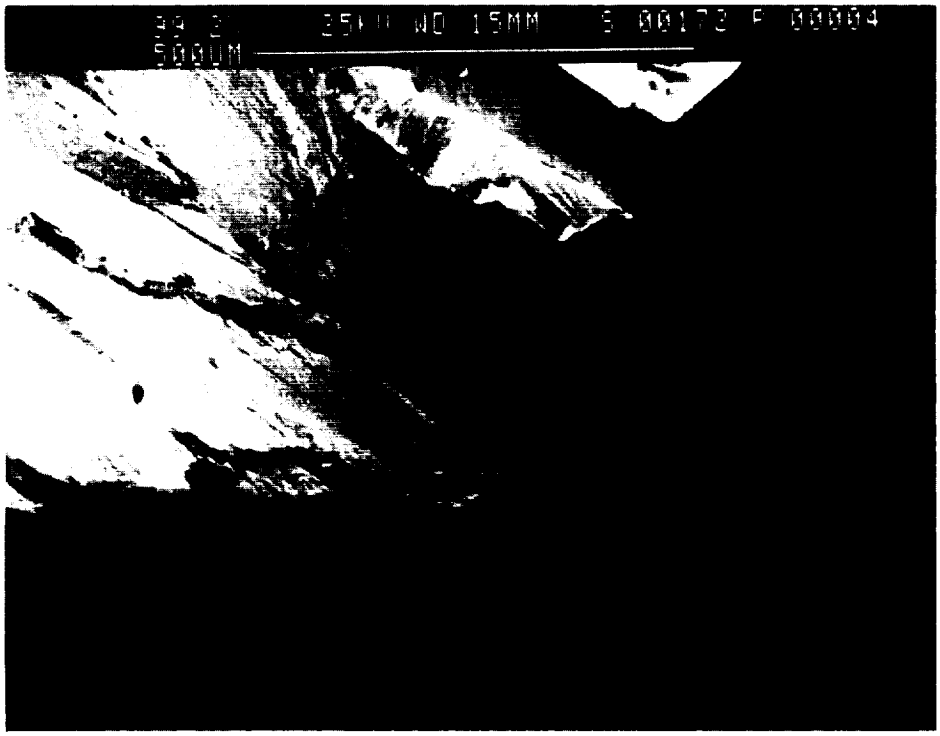

Figure 11d. Variation in Failure Micropore Morphology

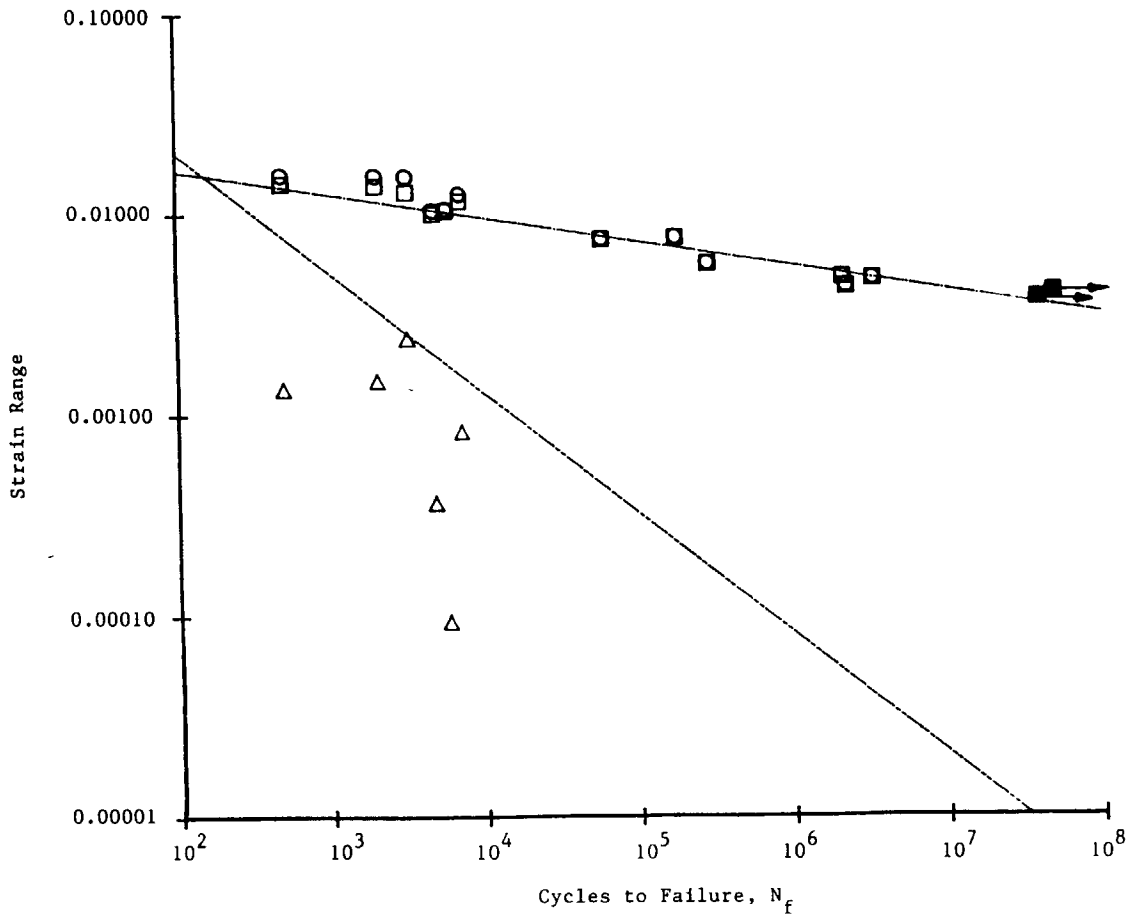

Figure 12. Universal Slopes Prediction of Fatigue Behavior

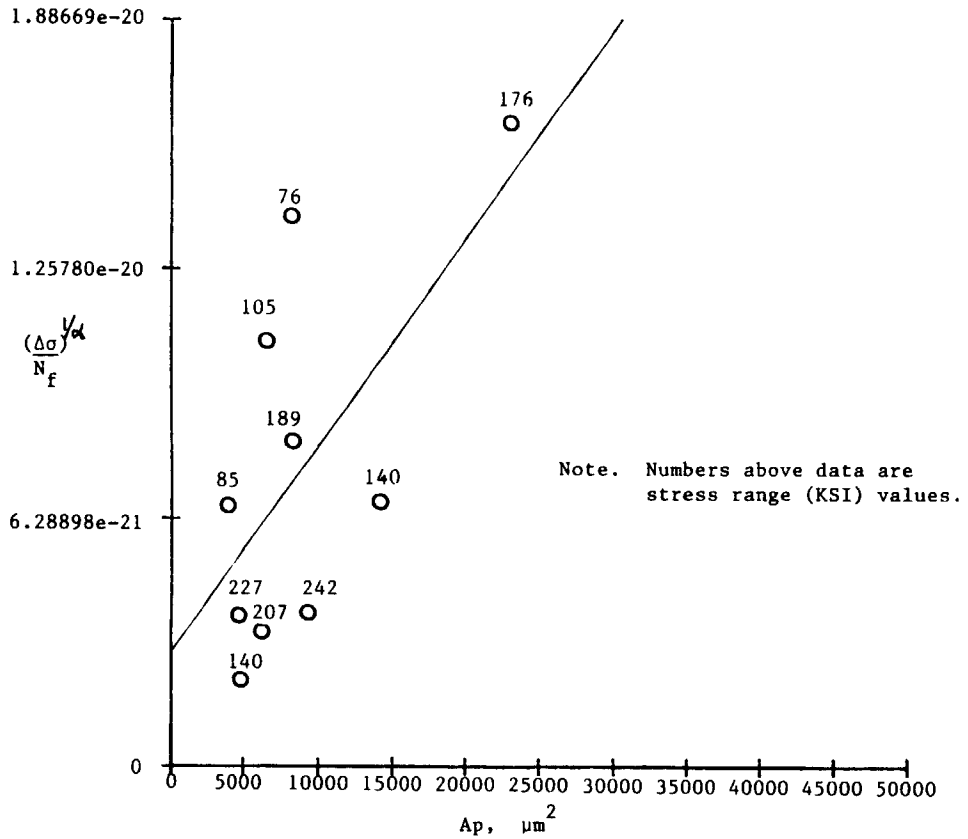

Figure 13. Fatigue Life Parameter vs. Microporosity Area

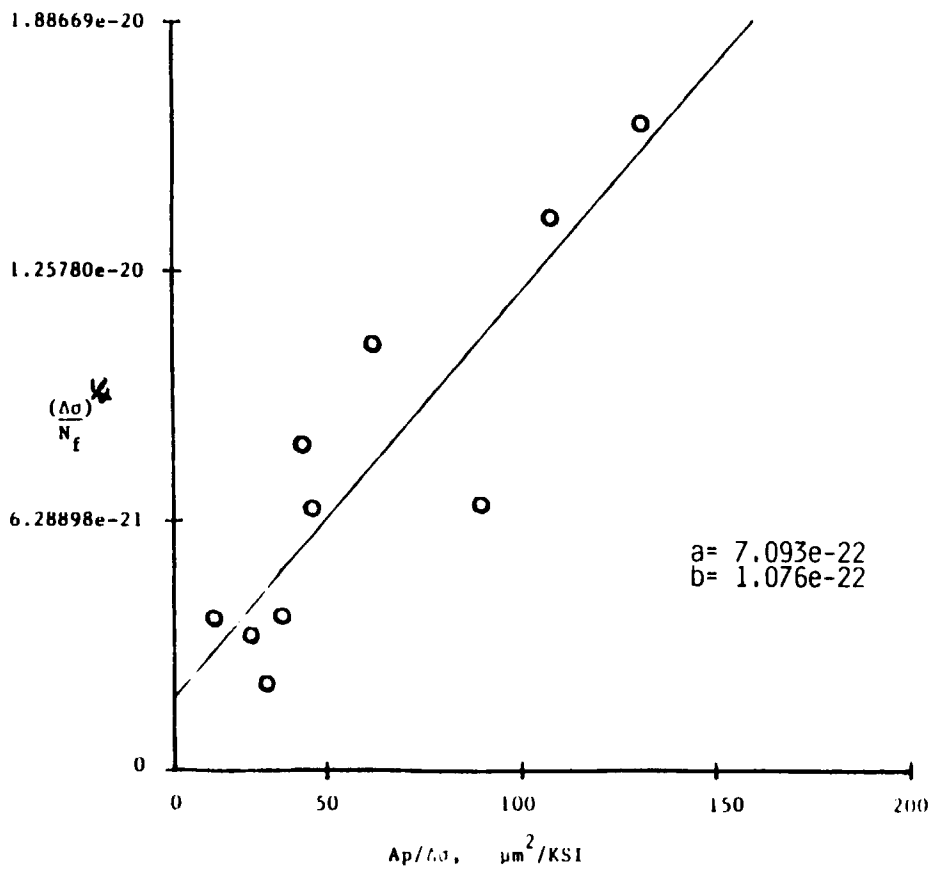

Figure 14. Fatigue Life Parameter vs. Microporosity Areas/Stress Range

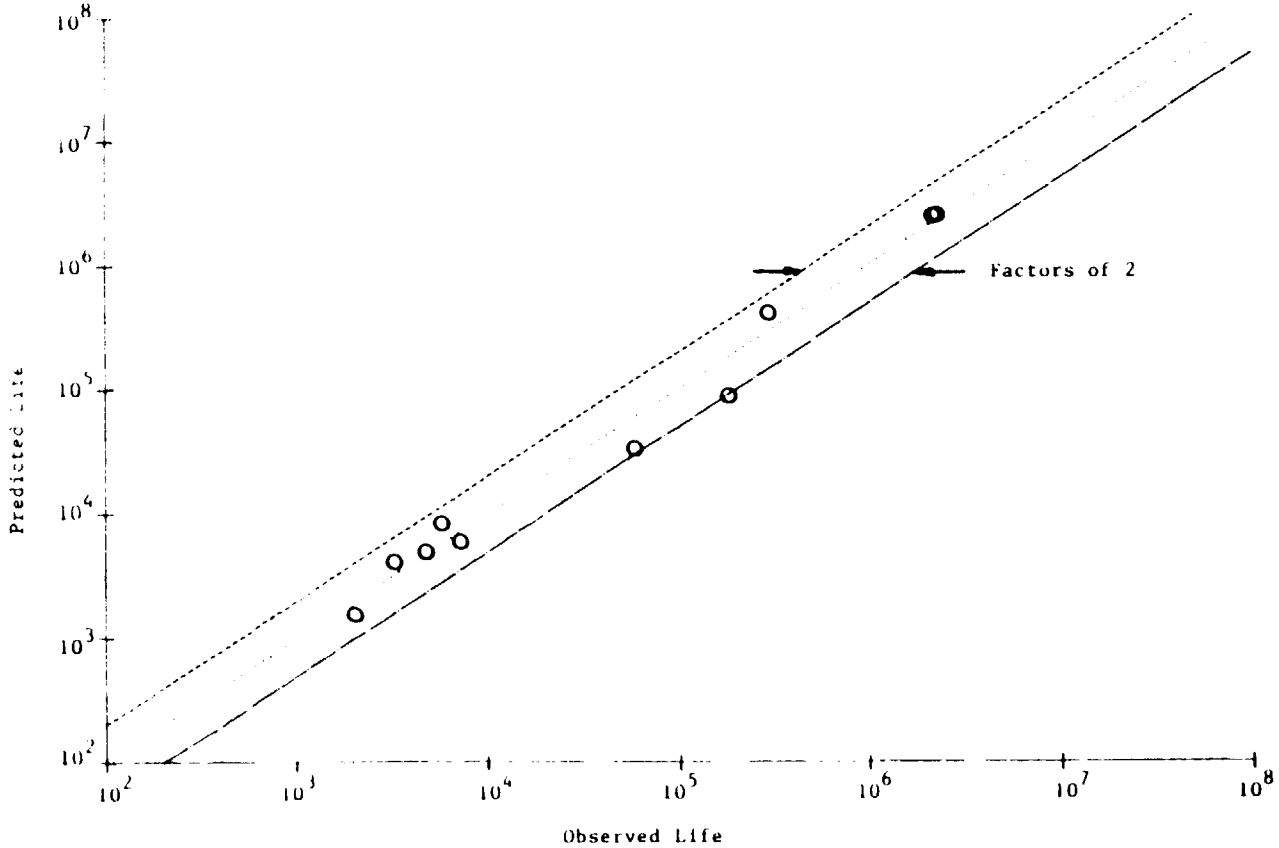

Figure 15. Predicted vs. Observed Life, Microporosity Effects Considered

Figure 16. PWA 1480: Observed Lives and Microporosity-Free Predictions

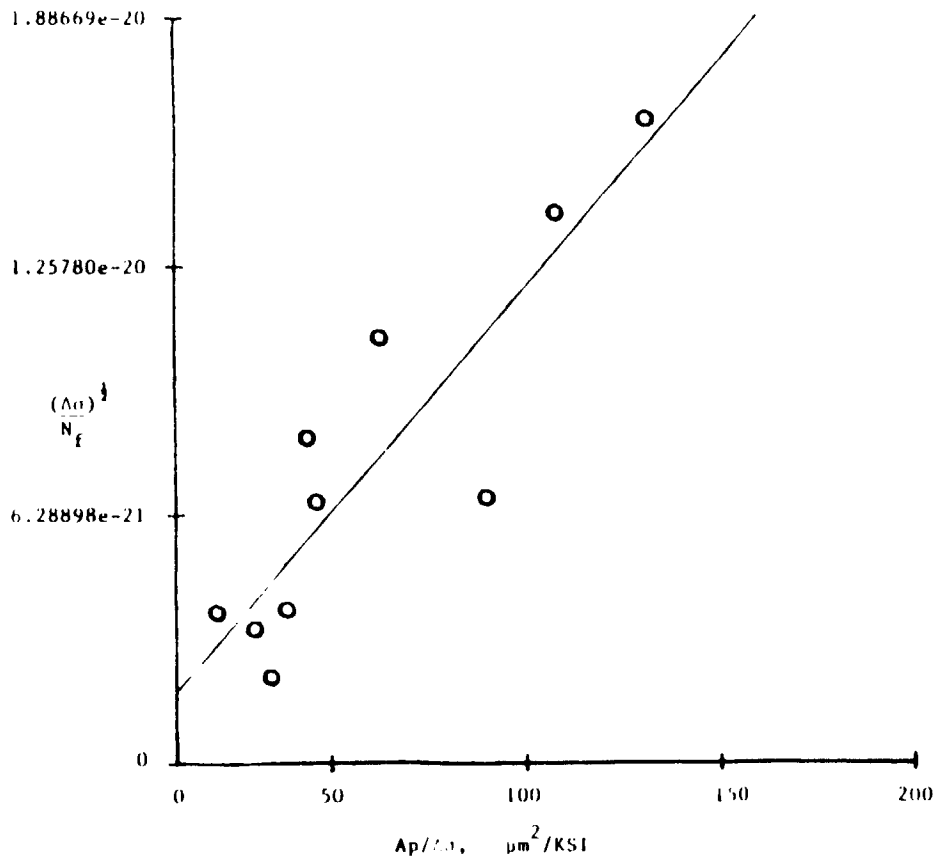

Figure 14. Fatigue Life Parameter vs. Microporosity Areas/Stress Range

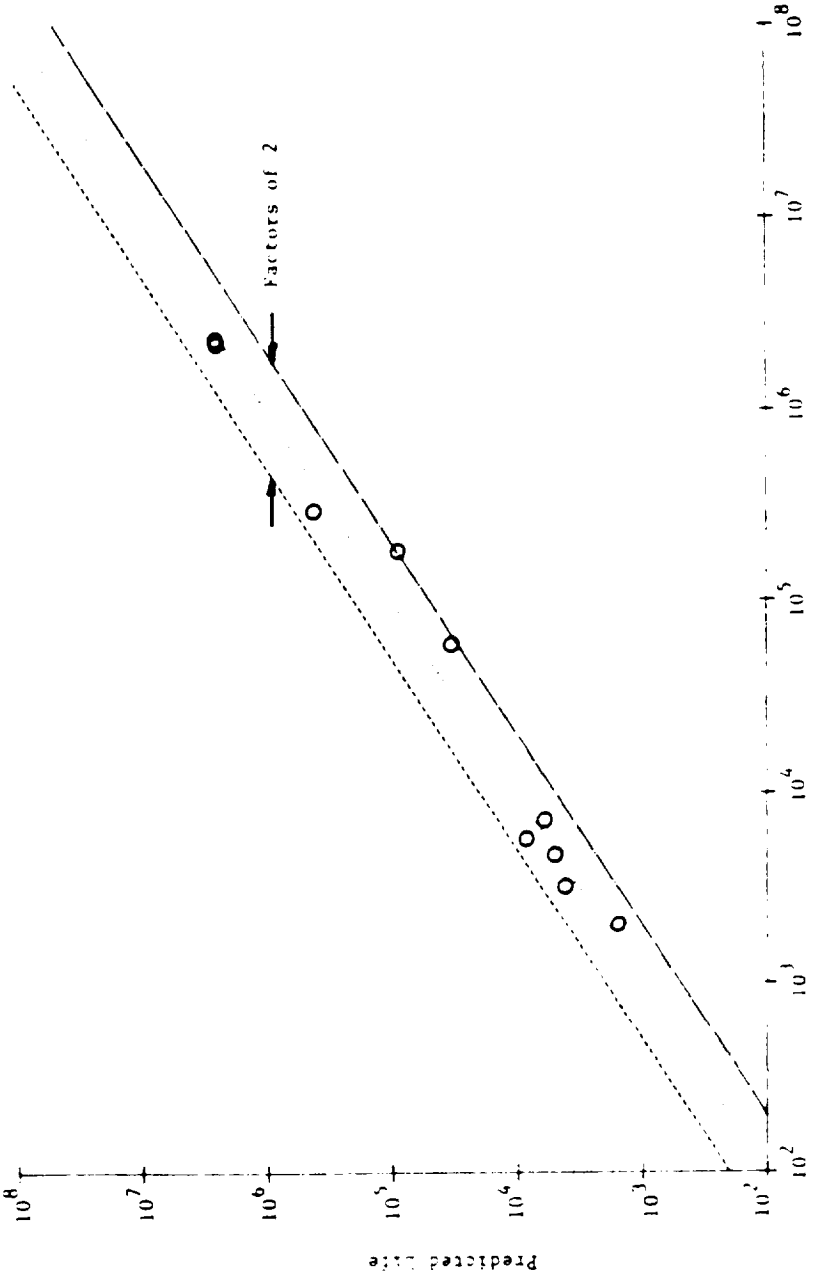

Figure 15. Predicted vs. Observed Life, Microporosity Effects Considered

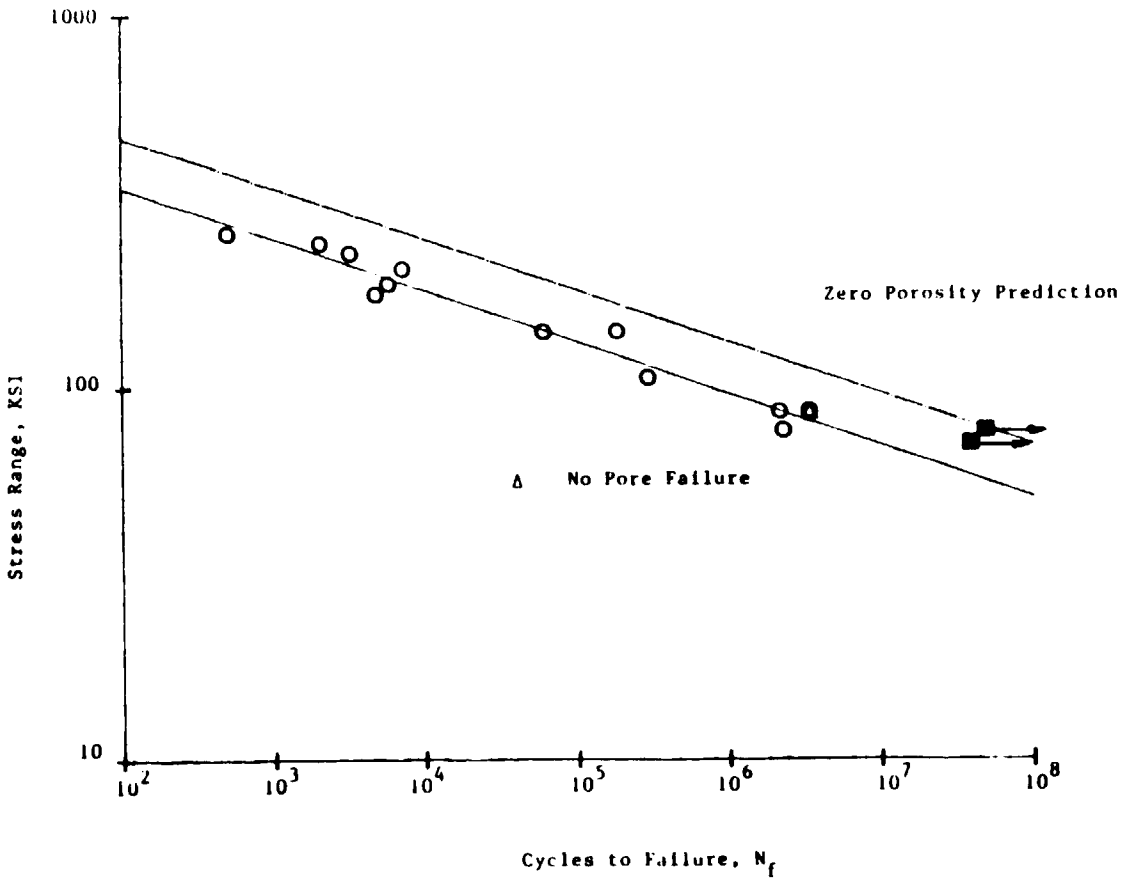

Figure 16. PWA 1480: Observed Lives and Microporosity-Free Predictions